TITLE: NUMERICAL STUDY ON THE IMPORTANCE OF THE TURBULENT INLET BOUNDARY CONDITION AND DIFFERENTIAL DIFFUSION IN A TURBULENT H_2/N_2/AIR JET DIFFUSION FLAME

Author: A. D'Ausilio, Department of Flow Heat and Combustion Mechanics, Ghent University, Ghent, Belgium, Alessandro.DAusilio@UGent.be, corresponding author

Author: I. Stankovic, Department of Flow, Heat and Combustion Mechanics, Ghent University-UGent, St.-Pietersnieuwstr. 41, 9000 Ghent, Belgium, Ivana.Stankovic@UGent.be

Author: B. Merci, Department of Mechanics of Flow, Heat and Combustion, Ghent University, St-Pietersnieuwstraat 41, 9000 Gent; and Postdoctoral Fellow of the Fund of Scientific Research - Flanders,Belgium. Bart.Merci@UGent.be

A. D'Ausilio*, I. Stankovic*, B. Merci*

alessandro.dausilio@ugent.be

* Ghent University – UGent, Department of Flow, Heat and Combustion mechanics, Belgium

Abstract

This work concerns numerical simulations of the turbulent H_2/N_2/air jet diffusion flame (Meier et al., 1996), using Large Eddy Simulations (LES) and Conditional Moment Closure (CMC) as combustion model. The study focuses on the impact of the Random Spots method (Kornev et al., 2007), adopted to describe the turbulence at the inlet, on the flow field. Furthermore the region where the contribution of differential molecular diffusion is relevant is determined through the analysis of the Scalar Dissipation Rate (SDR). The numerical results are discussed

through the analysis of Favre-averaged profiles of velocity, mixture fraction temperature and species along the centerline and at three axial locations.

Introduction

In the present study, we apply the Large Eddy Simulations (LES) technique with the first order Conditional Moment Closure (CMC) method (Klimenko et al., 1999) to a nitrogen-diluted hydrogen flame (H3 flame), studied by Meier et al. (1996). The chosen flame is well characterized and it is a standard benchmark case used in the Turbulent Non-premixed Flame workshop series (TNF). It has been studied previously both experimentally (Pfuderer et al., 1996) and numerically.

Pitsch et al. (1998) numerically examined the H3 flame to test the unsteady flamelet approach coupled with a standard k-ε model. Using the same flamelet libraries, Forkel et al. (2000) carried out LES simulations testing two different inlet boundary conditions. Panjvani et al. (2010), performing LES coupled with the Eddy Dissipation Concept (Ertesvag et al., 2000), identified the inflow boundary condition as the main cause of the discrepancies between experimental and simulation results.

The H3 flame studies reviewed so far did not take into account the differential diffusion (DD) effect, which according to Meier et al. (1996) is non-negligible. In the study of Maragkos et al. (2015), a new methodology was proposed to include differential diffusion effect in turbulent diffusion flames with good agreement with experimental data in regions where differential diffusion was expected. Pitsch (2000) discussed the effect of differential diffusion in turbulent diffusion flames identifying three possible criteria: (1) the existence of a laminar mixing layer in the near-nozzle region; (2) the molecular diffusivity being of the same order magnitude as the turbulent eddy diffusivity, which can be related criterion (1); and (3) the mixing layer thickness being smaller than the small turbulent eddies.

While differential diffusion may indeed be important for the flame at hand, it is not implemented in the present study. In other words, the conventional approach of equal diffusivity is adopted. Nevertheless, the region where its contribution is not negligible is

determined through the analysis of the Scalar Dissipation Rate, both in physical and mixture fraction space.

This study will assess the capability of the Random Spot method developed by Kornev et al. (2007), as turbulent inlet boundary condition, to describe the H3 flame flow field. This method is based on the idea that turbulent flow is a motion of turbulent spots of a certain size arising at random position at random times.

   The paper is divided into three parts. The first section deals with the mathematical description of the LES-CMC approach. The second section describes the experimental and computational details; with mainly attention to the inlet boundary condition. In the third section numerical results are discussed and compared to the experimental data. Mean flow fields, mixing fields and temperature fields, as well as fluctuations thereof, are discussed.

LES-CMC Modeling

The LES equations for mass, momentum and mixture fraction read (Poinsot et al., 2001):

$$\frac{\partial \bar{\rho}}{\partial t} + \frac{\partial (\bar{\rho} \tilde{u}_i)}{\partial x_i} = 0 \tag{1}$$

$$\frac{\partial \bar{\rho} \tilde{u}_i}{\partial t} + \frac{\partial (\bar{\rho} \tilde{u}_i \tilde{u}_j)}{\partial x_j} = -\frac{\partial \bar{p}}{\partial x_i} + \frac{\partial \tilde{\tau}_{ij}}{\partial x_j} - \frac{\partial \tau_{ij}^{sgs}}{\partial x_j} + \bar{\rho} g_i \tag{2}$$

$$\frac{\partial (\bar{\rho} \tilde{f})}{\partial t} + \frac{\partial \bar{\rho} \tilde{u}_i \tilde{f}}{\partial x_i} = \frac{\partial}{\partial x_i} \left(\bar{\rho} D \frac{\partial \tilde{f}}{\partial x_i} - \bar{\rho} J_i^{sgs} \right) \tag{3}$$

In the equations $\bar{\rho}$ is the filtered density, $\tilde{u}$ is the filtered velocity and $\tilde{f}$ is the filtered mixture fraction. Favre filtered averages are used for velocity and mixture fraction. The third term on the right hand side of the Eq.(2), $\tau_{ij}^{sgs} = \bar{\rho}(\widetilde{u_i \tilde{u}_j} - \tilde{u}_i \tilde{u}_j)$, is the sub-grid scale, SGS (residual)

stress tensor. Through this term the effect of the small scales is included. The sub-grid scale stresses are expressed according to the Boussinesq assumption as:

$$\tau_{ij}^{sgs} = \bar{\rho}\left(\widetilde{u_i u_j} - \tilde{u}_i \tilde{u}_j\right) = \mu_t \left[\left(\frac{\partial \tilde{u}_i}{\partial x_j} + \frac{\partial \tilde{u}_j}{\partial x_i}\right) - \frac{2}{3}\frac{\partial \tilde{u}_k}{\partial x_k}\delta_{ij}\right] \tag{4}$$

The turbulent viscosity, μ_t, is then modeled through the dynamic One Equation Model (Schumann, 1975):

$$\mu_t = \bar{\rho}c_k \Delta \tilde{k}^{\frac{1}{2}} \tag{5}$$

In Eq.(5) c_k is a model parameter, determined dynamically (Davidson, 1997), Δ is the cubic root of the LES cell volume and $\tilde{k}$ is the sub-grid scale turbulent kinetic energy.

In Eq.(3), $D = \nu/Sc$ is the diffusivity, where a constant Schmidt number Sc = 0.7 is used (Le = 1). In turbulent combustion, the hypothesis of equal diffusivities is based on the assumption that turbulence mixing is a far more dominant process than molecular mixing. As it is reported by Meier et al ((Stankovic, et al., 2013)) this assumption could be not fulfilled close to the combustion nozzle, and if there are any species in the mixture which diffuse faster than others (i.e. hydrogen), including the differential diffusion effect will determine a more accurate prediction of temperature and species concentration profiles.

$J_j{}^{sgs}$ is the scalar transport due to the sub-grid scale fluctuations, which is modelled as:

$$J_i{}^{sgs} = -D_t \frac{\partial \tilde{f}}{\partial x_i} \tag{6}$$

where D_t is the turbulent diffusivity: $D_t = \frac{\nu_t}{Sc_t}, \nu_t = \frac{\mu_t}{\rho}$ and Sc_t is turbulent Schmidt number.

A constant value of $Sc_t = 0.7$ is used throughout this work (Schmitt et al., 2011).

For combustion and turbulence – chemistry interaction, the first order CMC approach is adopted (Klimenko et al., 1999). The CMC model assumes that fluctuations of species mass fractions and enthalpy (or temperature) can be associated with the fluctuation of a single scalar, mixture fraction, in non-premixed combustion. This means that the transport equations are solved for the conditionally filtered scalars, with the conditioning on the mixture fraction.

Defining the conditionally filtered mass fraction of species as $Q_\alpha = \widetilde{Y_\alpha|\eta}, \ \alpha = 1, \dots n$, and the conditionally filtered enthalpy as $Q_h \equiv \widetilde{h|\eta}$, conditioned on the sample space variable, η, for mixture fraction, the three-dimensional CMC equations read:

$$\frac{\partial Q_\alpha}{\partial t} + \widetilde{u_i|\eta} \frac{\partial Q_\alpha}{\partial x_i} = \widetilde{N|\eta} \frac{\partial^2 Q_\alpha}{\partial \eta^2} + \widetilde{w_\alpha|\eta} + e_f \tag{7}$$

$$\frac{\partial Q_h}{\partial t} + \widetilde{u_i|\eta} \frac{\partial Q_h}{\partial x_i} = \widetilde{N|\eta} \frac{\partial^2 Q_h}{\partial \eta^2} + e_f \tag{8}$$

The terms in Eq.(7), starting from the first term on the left hand side, are: unsteady term, convection, micro-mixing, conditionally filtered chemical source term and sub-grid conditional flux. The latter accounts for the conditional transport in physical space and is modelled with the gradient model (Klimenko et al., 1999; Zhang et al., 2016):

$$e_f = \nabla \cdot (D_t \nabla Q_\alpha) \tag{9}$$

6

Conditional fluctuations of the reactive scalars are assumed much smaller than unconditional fluctuations and are neglected in a first order closure of the chemical source term using the conditionally filtered scalars:

$$\widetilde{w_\alpha | \eta} = w_\alpha(Q_\alpha, Q_h) \tag{10}$$

$\widetilde{u_i | \eta}$ and $\widetilde{N | \eta}$ correspond, respectively, to be conditionally filtered velocity and conditionally filtered scalar dissipation rate. These terms are unclosed and therefore require modelling. The conditional velocity is assumed equal to the local unconditional filtered velocity, $\widetilde{u_i | \eta} = \widetilde{u_i}$ (Garmory et al., 2013; Stankovic et al., 2013). The conditionally filtered scalar dissipation rate (SDR) is modeled by the Amplitude Mapping Closure (AMC) model (O'Brien et al., 1991):

$$\widetilde{N | \eta} = \frac{\widetilde{N} G(\eta)}{\int_0^1 \tilde{P}(\eta) G(\eta) d\eta} \tag{11}$$

In Eq. (11), $\tilde{P}(\eta)$ is the Filtered probability Density Function (FDF), assumed to have a β-function shape, and $G(\eta)$ is prescribed to be an error function:

$$G(\eta) = \exp(-2[erf^{-1}(2\eta - 1)]^2) \tag{12}$$

The filtered scalar dissipation rate $\widetilde{N}$ is calculated through (Pera et al., 2006):

$$\widetilde{N} = \widetilde{N_{res}} + \widetilde{N_{sgs}} = D \frac{\partial \tilde{f}}{\partial x_i} \frac{\partial \tilde{f}}{\partial x_i} + \frac{1}{2} C_N \frac{\mu_t}{\Delta^2} \widetilde{f''^2} \tag{13}$$

In Eq. (13), C_N is a constant chosen equal to 42 (Garmory et al., 2013), and the mixture fraction variance $\widetilde{f''^2}$ is calculated as:

$$\widetilde{f''^2} = C_V \Delta^2 \nabla \tilde{f} \cdot \nabla \tilde{f} \tag{14}$$

An important finding is that conditional variables vary much less in physical space than unconditional quantities. Therefore, in order to take full advantage of the LES-CMC formulation, it is common practice to solve the CMC equations on a coarser mesh (Garmory et al., 2015; Stankovic et al., 2013). This approach is followed here. It implies that the flow field information from the LES resolution must be transferred to the CMC resolution and an averaging procedure has to be used. As in previous studies (Stankovic et al., 2013), mass weighted averaging over all LES cells associated with one CMC cell is used for mixture fraction, mixture fraction variance and scalar dissipation rate. For the scalar dissipation rate, the AMC model is applied at the CMC resolution in order to obtain the conditional scalar dissipation rate. The filtered velocity and turbulent diffusivity do not undergo an averaging operation: their values at CMC faces are interpolated using the LES face properties.

Using the local FDF, the resolved enthalpy and species concentrations are calculated from the conditional averages in each LES cell at each time step by integrating over mixture fraction space:

$$\tilde{h} = \int_0^1 \widetilde{h|\eta} \tilde{P}(\eta) d\eta \, , \, \widetilde{Y_\alpha} = \int_0^1 \widetilde{Y_\alpha|\eta} \tilde{P}(\eta) d\eta \tag{15}$$

From the filtered enthalpy and species mass fractions values the filtered density and temperature are provided to the LES resolution and the flow field is updated accordingly. This bi-directional data communication between the fine LES mesh and the course CMC mesh is illustrated in Figure.1 (Zhang et al., 2016).
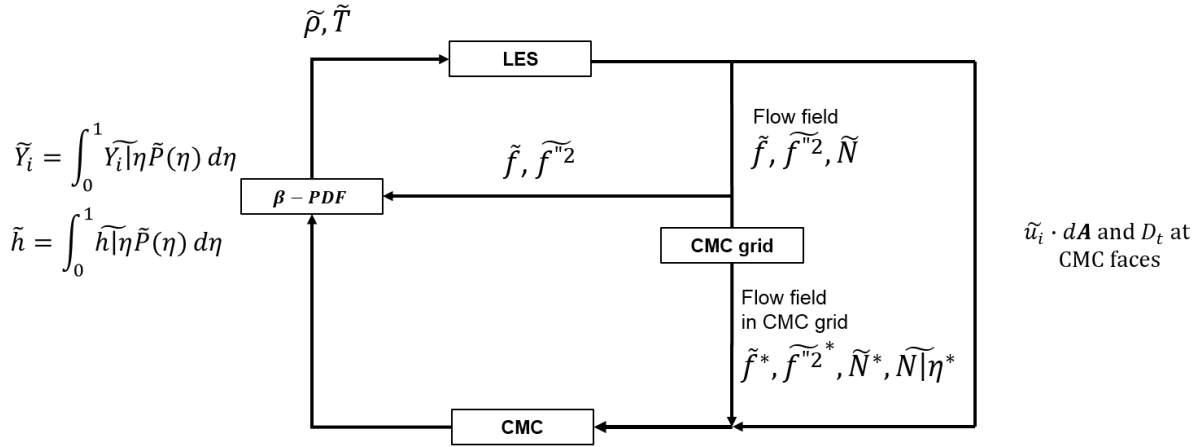
$$\tilde{Y}_i = \int_0^1 \widetilde{Y_i|\eta} \tilde{P}(\eta)\, d\eta$$

$$\tilde{h} = \int_0^1 \widetilde{h|\eta} \tilde{P}(\eta)\, d\eta$$

Figure 1. Coupling of LES and CMC (Zhang et al., 2016)

Test Case and Numerical Setup

The non-premixed jet flame is a H_2 flame, diluted with 50% vol N_2. The experimental data set, available in literature (Meier et al., 1996), includes simultaneous measurements of velocity, temperature, the major species mass fractions (O_2, H_2, N_2, H_2O), and the mass fraction of OH. In the experiment the burner is a straight tube with inner diameter $d = 8\ mm$ centered in a co-flow emanating from a contoured nozzle. The co-flow air velocity is $0.2\ m/s$. Both co-flow air and fuel exit temperature are 298 K.

At the nozzle exit the bulk velocity is 34.8 m/s and Re = 10000. The mean velocity and the Reynolds-stress components are known only on the axis and as stated by Forkel et al. (2000), the assumption of fully developed turbulent pipe flow might not be correct. The stoichiometric mixture fraction for this fuel composition is $f_{st} = 0.31$ and the adiabatic flame temperature is equal to $T = 2040$ K.

The simulation domain consists of a cylinder with radius equal to 18.75 d and length equal to 81.25 d. The LES mesh has a structured O-ring arrangement. The inlet patch is divided into 4×4 cells in the rectangular section and 16×16 in the cylindrical. The co-flow patch is divided into 16×70 cells. Axially the domain is discretized using 500 cells. This discretization gives a total number of 0.688 million cells for the whole domain.

The CMC grid consists of 50 (axial direction) $\times 10 \times 10$ cells. The mixture fraction space is discretized into 101 bins clustered around the stoichiometric mixture fraction. CMC equations are solved using an in-house finite-volume code (Garmory et al., 2015; Zhang et al., 2016) .

The LES equations are solved using the reactingFoam solver, available in OpenFOAM$^{\circledR}$ code (Chrsitopher, 2015). They are discretized using the built-in numerical schemes available in OpenFOAM$^{\circledR}$. They are advanced in time using a first order bounded implicit 'Euler' scheme. The convective terms for the momentum equation are second order centrally differenced using 'Gauss linear' interpolation. For the convective term in the mixture fraction equation, a Gauss linear scheme that limits towards upwind in regions of rapidly changing gradient is used. The gradient terms are evaluated through the standard Green-Gauss method while the diffusive terms are centrally differenced and corrected for the non-orthogonality of the mesh with 'Gauss linear corrected'. The PISO algorithm is used for velocity-pressure coupling.

The CMC code is a finite volume solver, built as an extension of the reactingFoam solver (Garmory et al., 2015). Full operator splitting is used for the terms in Eqs. (7) and (8) in order to reduce the computational load. The conditional chemical source term is calculated using solver VODPK (Brown et al., 1989). The micro-mixing term is calculated with the Tridiagonal Matrix Algorithm (TDMA) method. The first-order upwind and second-order central

differencing schemes are used for conditional convection and sub-grid conditional flux terms of Eqs. (7) and (8). Time integration is performed by a first-order Euler scheme.

The H_2/O_2 reaction mechanism as presented by Li et al. (2004) is used in the present study. It consists of 19 reversible elementary reactions between 9 species ($H_2, N_2, O_2, H_2O, H, O, OH, HO_2, H_2O_2$). The chemical source terms in Eq. (7) were computed using the CHEMKIN® libraries.

The simulation time step is dynamically adjusted so that the Courant number never exceeds 0.35. The execution time needed to simulate 2s of combustion is approximately four weeks. The simulations are performed on an Intel Xeon E5-2680v2 10-core 2.7GHs cluster.

The overview of the boundary conditions (BC) for the velocity, pressure, temperature and mixture fraction as implemented in OpenFOAM® (Christopher, 2015), is provided in Table 1.

Table 1. Boundary Conditions implemented in OpenFOAM®

	U [m/s]	p [Pa]	T [K]	f [-]
Inlet	Random Spot method	zeroGradient	fixedValue=298	fixedValue=1
Co-flow	FixedValue=0.2	zeroGradient	fixedValue=298	fixedValue=0
Sides	Symmetry	Symmetry	Symmetry	Symmetry
Outlet	pressureInletOutletVelocity	totalPressure	inletOutlet	inletOutlet

In LES, the setting of the turbulent inflow conditions is of paramount importance and not trivial. In this work the method of Random Spots is used (Kornev et al., 2007).

Through this method, at each time step, M spots are randomly positioned in the space. The random spots size is chosen proportional to the integral length scale; with this assumption, the inflow signal is generated with a prescribed two-point space autocorrelation function. Every i[th]

spot has a velocity distribution and the velocity fluctuations at inlet boundary are calculated as sum of velocities induced by each spot. As last step, the velocity fluctuations undergo a linear transformation (Lund et al., 1998) so that they also have prescribed Reynolds stresses.

Therefore in order to use this boundary condition at the inlet, the mean velocity profile, the integral length scale and Reynolds stress tensor should be provided. They can either be given at the inlet as the average value or such that their profiles are described by means of a discrete list of values imposed at each inlet cell centre.

The inlet mean velocity profile is assumed to follow the 1/7 power law.

The integral length scale, which is proportional to the spot size is set equal to 0.001 m ($\sim 0.12\ d$). The Reynolds stress tensor profile for each component is assumed to follow the radial profile of the turbulent jet in the self-similar region, hence neglecting the contribution due to the reaction (Pope, 2000).

It is noted that the method does not generate turbulence structures that are correlated in time (i.e., there is no notion of turbulence integral time scale). Improving this is beyond the scope of the present study.

At the side of the domain the 'free slip' boundary condition has been chosen. Through this the convective flux and the diffusive flux are zero at boundary, preventing any undesired side-outflow.

Results

Differential Diffusion effect

As reported by Meier et al. (1996) the investigated flame has a strong differential diffusion effect close to the nozzle, but this effect vanishes approximately at x/d=20 when transport by turbulence dominates molecular diffusion.

The DD effect can be analysed through the profile of the Scalar Dissipation Rate at stoichiometric mixture fraction ($SDR_{st}=2N$) as function of the nozzle distance (Figure 2). The SDR_{st} represents the rate of the molecular scalar mixing in the reaction zone. High SDR_{st} values indicate a very thin mixing layer. The significant difference between SDR_{st} values close to the nozzle and downstream, as shown in Figure 2, suggests that mixing could be controlled by the molecular diffusion at low x/d and by the small scales of turbulence at high x/d.
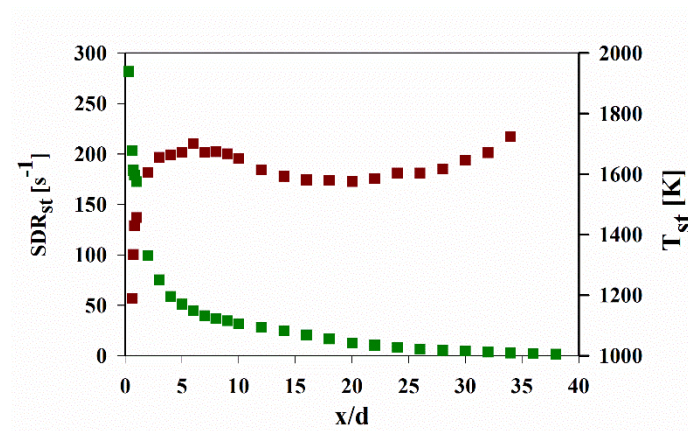
Figure 2. Unconditional scalar dissipation rate (square) and temperature (circle) at the stoichiometric mixture fraction along the centerline.

To be more precise, mixing will be controlled by molecular diffusion when the mixing layer is smaller than the Kolmogorov scale (Pitsch, 2000). The mixing layer can be calculated as (Peters, 2000):

$$l_m = \left(a \frac{\left(f_{st}^2 \left(1 - f_{st}^2\right)\right)}{SDR_{st}} \right)^3 \tag{17}$$

In Eq. (17), a is a small parameter defined as the ratio between the mixing length and the integral length scale and f_{st} the stoichiometric mixture fraction (Li et al., 2004).

The Kolmogorov scale can be calculated as (Johnson et al., 1993):

13

$$\lambda = L(Re_t)^{3/4} \qquad (18)$$

Where L is the local integral length scale, chosen equal to $0.25d_{loc}$ (d_{loc} : local jet diameter) and

Re_t is the turbulent Reynolds number defined as $Re_t = \dfrac{u'L}{\mu_{mix}}$.

The ratio of the mixing layer thickness and the Kolmogorov length scale is reported in Figure

3 . For $x/d < 15$ the ratio is below 1. Therefore, in this region the different molecular species

are transported also by molecular diffusion and the hypothesis of Lewis number equal to unity

can strongly affect temperature and species predictions.
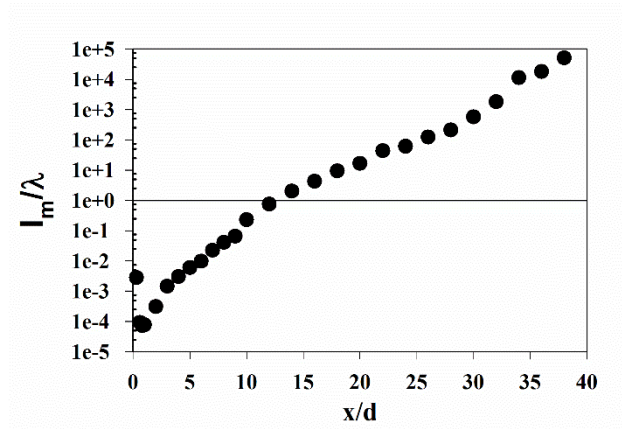
Figure 3. Ratio between the mixing length and the Kolmogorov scale along the contour of

the stoichiometric mixture fraction.

The effect of the high scalar dissipation rate in the near-nozzle region can be also examined in

the mixture fraction space. To this purpose the conditional profiles for temperature and

hydrogen mass fraction are reported in Figure 4.
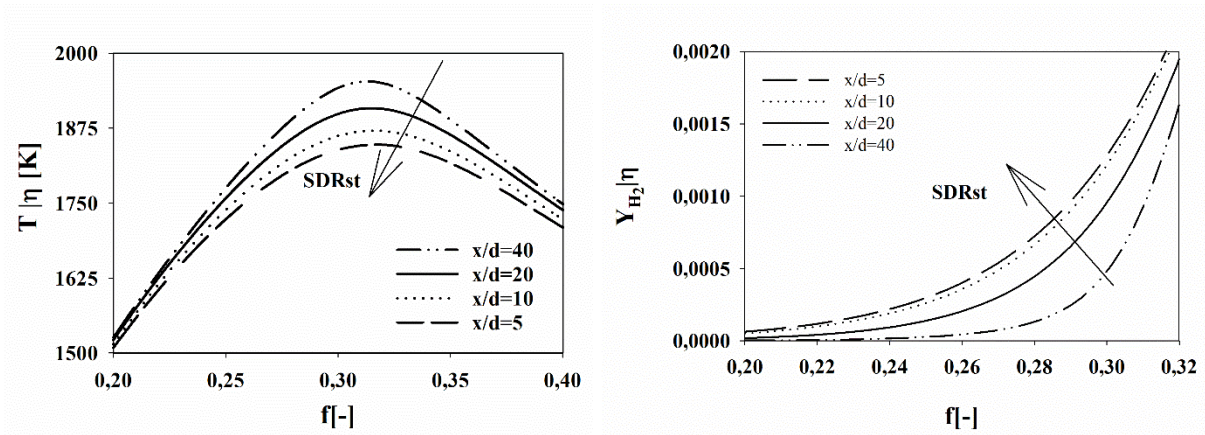
Figure 4. Conditional profiles for T (Left) and H_2 mass fraction (Right) as function of

mixture fraction at different distances from the nozzle.

In the CMC equations (Eqs. (7) and (8)) the scalar dissipation rate appears in the micro-mixing

term and acts as a diffusion coefficient in mixture fraction space. High scalar dissipation rate

values decrease the mixing time. The consequence is an increase of hydrogen at the oxygen

rich side and a decrease of the flame temperature, as can be seen in Figure 4. From experiments

the maximum temperature at x/d=5 is equal to 1950K. The conditional maximum temperature

at this location is equal to 1840K and after the integration over mixture fraction space through

Eq. (15) its value is equal to 1682K. The error between experiments and simulation result is

about 14 %.

Flow Field and Flame Structure

Figure 5 gives an overview of the contours of time averaged temperature and velocity. Time

averaging starts after 0.5 s and statistics are collected over a period of 1.5 s. The iso-lines of

the stoichiometric mixture fraction, the flame length L_f/d, and the position of the measured

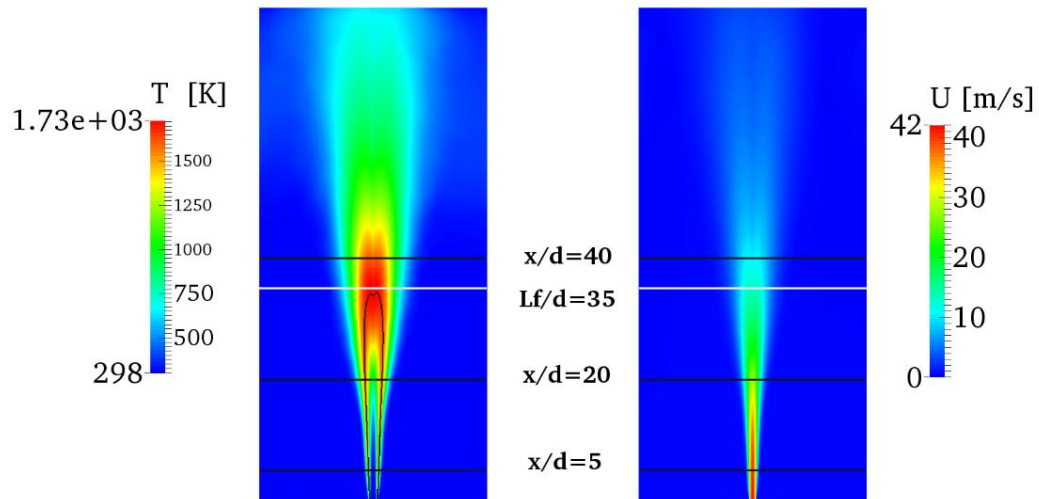radial profiles are indicated as well.

Figure 5. Time-averaged contour plots of temperature [K] (Left) and velocity [m/s] (Right)

In Figure 6 (left) a comparison of the mean and rms velocity along the centerline with the experimental data is reported. The errors are quantified in Table 2.
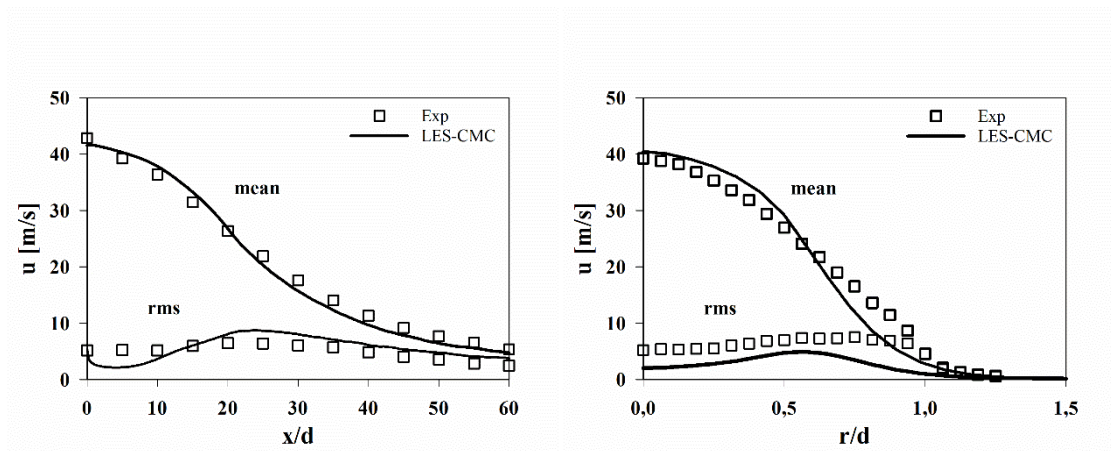

Figure 6. Left: Comparison of mean velocity and rms at the centerline with experimental data. Right: Radial Favre averaged velocity profiles at locations *x/d = 5*
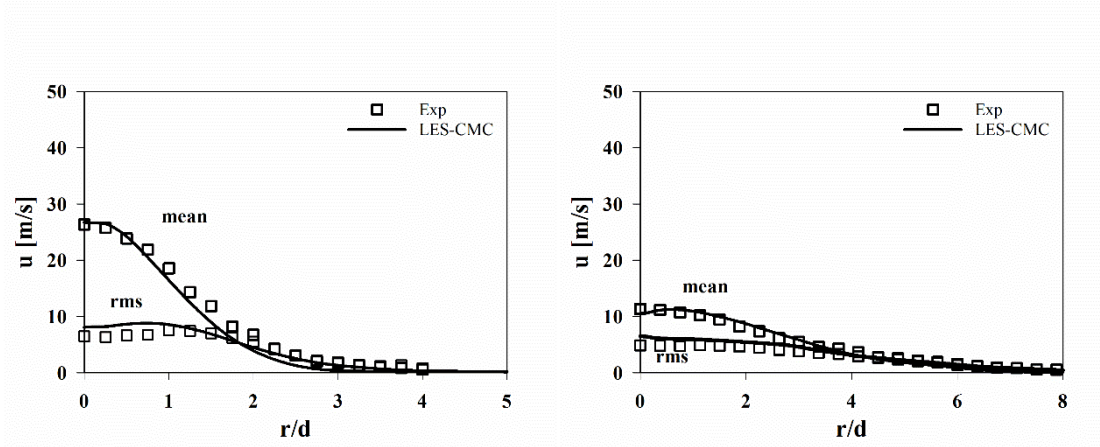
Figure 7. Radial Favre averaged velocity profiles at locations $x/d = 20$ (Left) and $x/d = 40$ (Right)

The error for the average velocity remains below 10 %, while for velocity rms the maximum error, obtained at the nozzle exit, is about 60%. The experimental rms remains almost constant at the centerline while in the numerical results the rms drops from the initial value given through the inlet boundary condition. This is probably related to the insufficiently realistic turbulence representation by the Random Spots method for the case at hand, in particular due to the lack of temporal correlation between the generated random spots. From $x/d\sim15$ onward the rms value increases again. Nevertheless, even downstream the error between numerical results and experimental data remains large (albeit that also experimental uncertainty is typically larger for rms values).

Table 2. Error analysis of the velocity and rms. along the centerline

x/d	U^{exp} [m/s]	U^{sim} [m/s]	U Err (%)	rms^{exp} [m/s]	rms^{sim} [m/s]	rms Err (%)
5	39.3	40.4	3.0	5.2	2.1	60.9
10	36.4	38.3	5.3	5.9	3.2	38.8
20	26.4	28.9	9.7	6.5	7.1	9.5
30	17.6	16.9	4.3	6.1	8.1	32.1
40	11.4	10.2	9.9	4.9	6.7	26.8

The radial profiles at three axial locations, which represent the near-nozzle region ($x/d = 5$) the flame region ($x/d = 20$) and the downstream region ($x/d = 40$), are reported in Figure 6 (right) and Figure 7. At $x/d = 5$ the level of velocity fluctuations (rms) obtained in the numerical simulations is low. This may be due to the absence of temporal correlations between the random spots, as mentioned. In the work of Forkel et al. (2000) it is shown that when inlet profiles, generated by separate LES pipe flow simulations, are imposed, good agreement is observed with experiments. A drawback of that method is the high additional computational cost for these separate LES pipe flow simulations. A similar drawback obviously applies if the entire burner is simulated.

The Random Spot method is in this sense an useful and advantageous tool, considering that chemistry plays a stronger weight in terms of computational power when an advanced combustion model, such as the CMC method, and a detailed chemical mechanism are used. Another advantage of the method is universality with respect to the inlet grid what is not the case in other analogous methods (Klein et al., 2003).

The profile from the simulations is narrower than the experimental data at $x/d = 20$ (Figure 7 left). This is in line with the drop of turbulence in the simulations as mentioned above: less turbulent diffusion leads to a slower velocity decay on the centreline and less wide profiles.

Further downstream ($x/d = 40$) qualitatively good agreement with experimental results is observed. At this location the influence of the inlet is not significant anymore; the sub-grid scale model, together with the LES mesh resolution, is dominant.

Despite the differences in terms of flow field as discussed (Figs. 6 and 7), the flow field measurements are considered well reproduced when the Random Spot is used. In D'Ausilio et al. (2017) the flow field results have been compared to what is obtained when White Noise is imposed at the inlet. As expected, with White Noise turbulence dies completely, before it is created again by the shear stresses at the edge of the jet. Using the Random Spot method as

synthetic turbulence at the inlet, this is not the case, even though the turbulence intensity still drops, compared to the value imposed at the inlet.
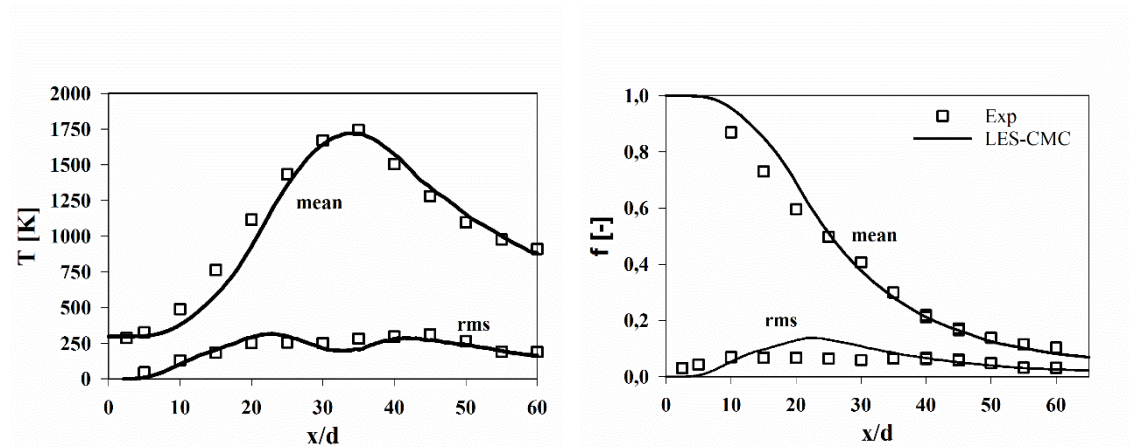

Figure 8. Comparison of mean and rms temperature (Left), mixture fraction (Right)
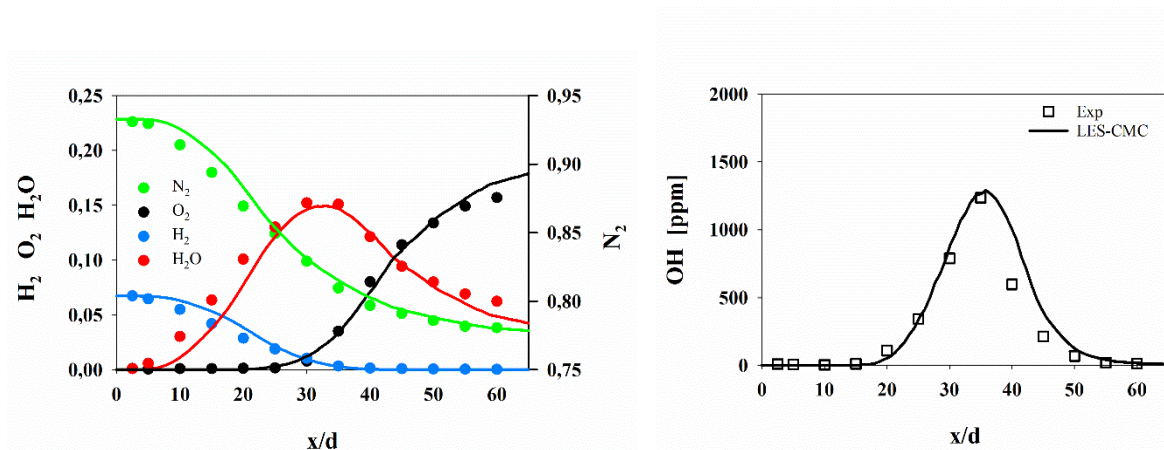

Figure 9. Comparison of mean major species mass fraction (Left) and *OH* mass fraction (Right) at the centerline with experimental data

The mean and rms values of temperature and mixture fraction along the axis are plotted in Figure 8. The maximum temperature is reached in the experiments at location $x/d = 35$, where the stoichiometric mixture fraction $f_{st} = 0.31$ is obtained. The calculated maximum temperature location is shifted slightly upstream, with deviation between experimental and simulation location value as low as 3%. An error analysis of the position and the value of the maximum

flame temperature, together with their values at the centreline, is presented in Table 3. The agreement behind the maximum is good, with the maximum error equal to 7% at $x/d = 50$. Upstream of the maximum, on the other hand, there is an under-prediction of temperature by approximately 150 K. This large discrepancy is related to the mixture fraction over-prediction in the same region. The mixture fraction variance drops to almost zero close to the nozzle exit and the mixture fraction decay at the centreline does not follow the experimental trend well. Again this is in line with the aforementioned unrealistic drop in turbulence. Since temperature and species values strongly depend on mixture fraction, the (in)accuracy of mixture fraction determines the (in)accuracy of their results.

Table 3. Error analysis on the position and value of the maximum flame temperature at the centreline

x/d Exp.	x/d Sim.	Err (%)
35.0	34.1	2.6
T_{max} **Exp.**	T_{max} **Sim.**	Err (%)
1745.7	1722.3	1.3

The numerical results of Favre-averaged mean values of H_2, O_2, N_2, H_2O and the radical OH mass fractions along the centreline are shown in Figure 9. Main deviation from measurements are observed before 20 nozzle diameter for major species; this is in line with the mixture fraction over-prediction (Figure 8).

The mean values of temperature and mixture fraction at the same axial locations as used for the mean velocity are reported in Figure 10. At $x/d = 5$ the differential diffusion effect, discussed above and not included in this study, is the reason for the difference between simulation and experiments around the maximum temperature position. At $x/d = 20$, the temperature is under-predicted both at the rich and lean side of the flame. The global temperature over-prediction at

x/d = 40 is a direct consequence of global over-prediction of the mean mixture fraction at that location.

An error analysis of the absolute value and the position of the maximum flame temperature obtained at various downstream locations in the numerical simulation is presented in Table 4.
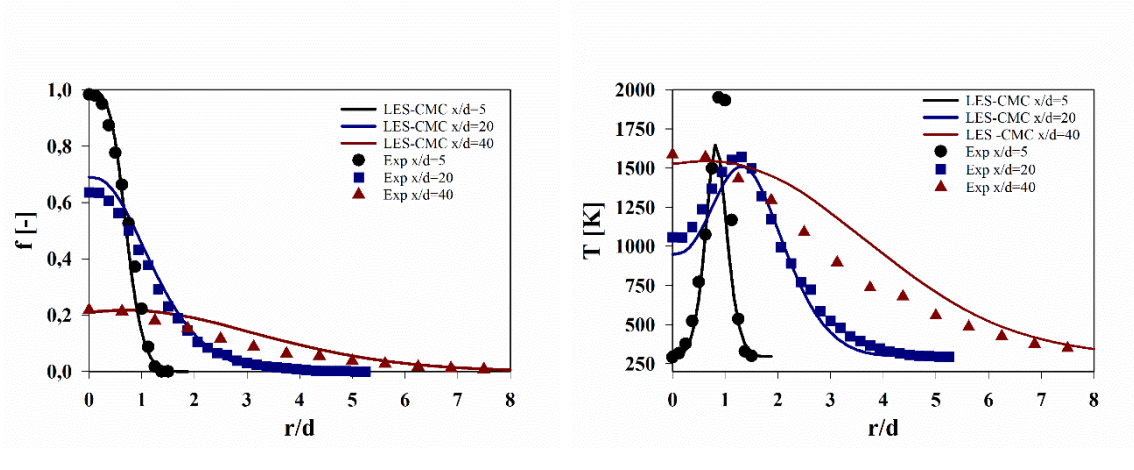

Figure 10. Radial profiles of Favre averaged mixture fraction (Left) and temperature (Right)

at locations *x/d* = 5, *x/d* = 20, *x/d* = 40

Table 4. Error analysis on the position and value of the maximum flame temperature at

different axial locations

x/d	T_{max}^{exp}[K]	T_{max}^{sim} [K]	Err. (%)	r/d^{exp}	r/d^{sim}	Err.(%)
5	1950	1682	13.7	0.9	0.8	6.3
10	1701	1670	1.8	1.1	1.0	12.9
20	1646	1568	4.7	1.3	1.3	1.6
30	1644	1633	0.7	0.9	1.2	30.9

The numerical results of Favre-averaged mean values of H_2, O_2, N_2, H_2O and the radical OH mass fraction at *x/d* = 5 are shown in Figures 11 and 12. These profiles confirm that the flow

field prediction has an important impact on the predictions for the species. The H_2 profile, e.g., shows strong analogy with the velocity profile shape at the same location.
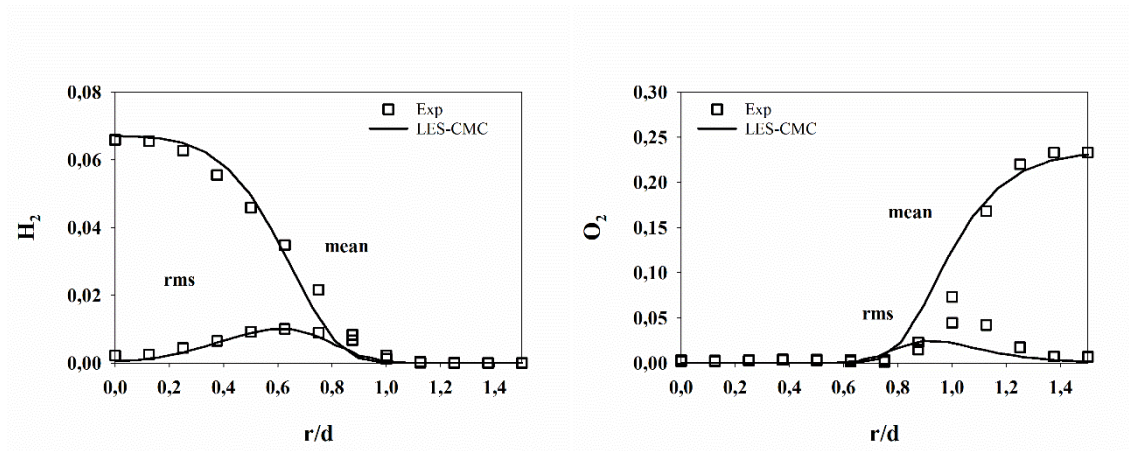

Figure 11. Favre averaged species mass fraction at location $x/d = 5$ for H_2 (Left) and O_2 (Right)
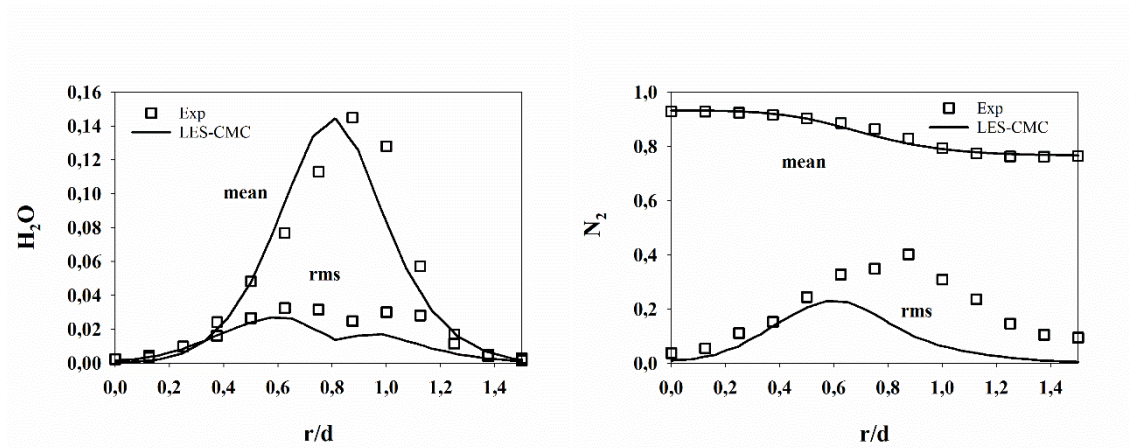

Figure 12. Favre averaged species mass fraction at location $x/d = 5$ for H_2O (Left) and N_2 (Right)

The simulation results of Favre-averaged mean values of H_2, O_2, N_2, H_2O and the radical OH mass fraction at $x/d = 20$ are shown in Figures 13 and 14. Overall, the predicted results agree well with the experimental data, illustrating that differential diffusion is no longer important from this location onward. Similar discrepancies as discussed for the temperature profile, are observed for H_2O (mass fraction slightly low). Moreover the H_2 mass fraction over-prediction

at the rich side of the flame is in line with the higher mixture fraction values reported above in the same region. The radial profile of the radical *OH* mass fraction, shown in Figure 15 (left), has a lower maximum value than the measurements. Nevertheless the reaction zone is well described if we consider that the *OH* radical is mostly found in the correct zone. Here the reaction zone already broadens while upstream it is very narrow until almost 15 nozzle diameters, as reported in the instantaneous contour plot in Figure 15.
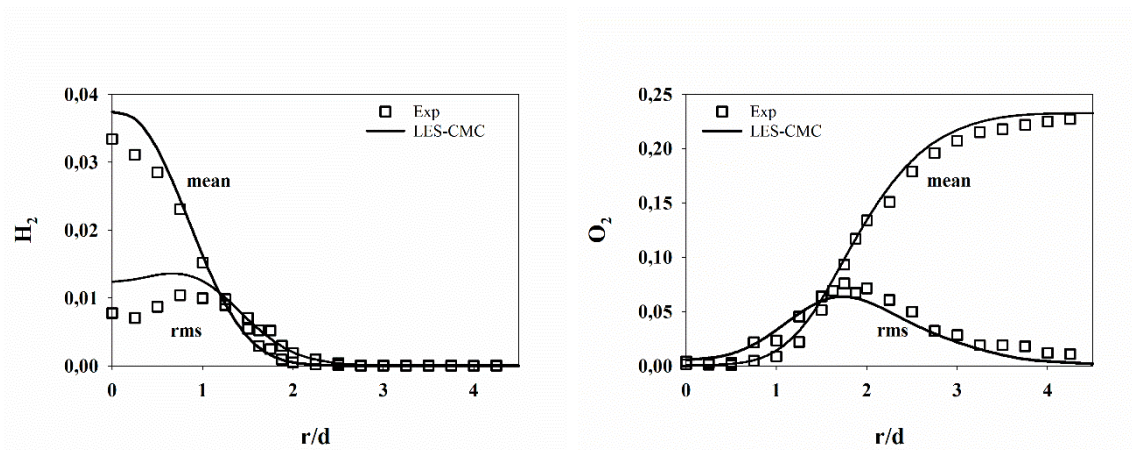

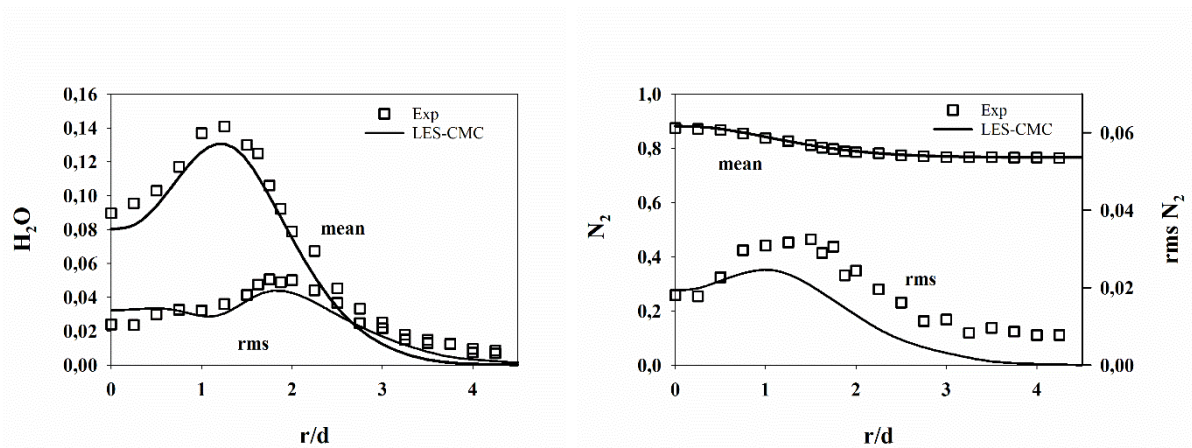**Figure 13.** Favre averaged species mass fraction at location $x/d = 20$ for H_2 (Left) and O_2 (Right)

Figure 14. Favre averaged species mass fraction at location $x/d = 20$ for H_2O (Left) and N_2 (Right)
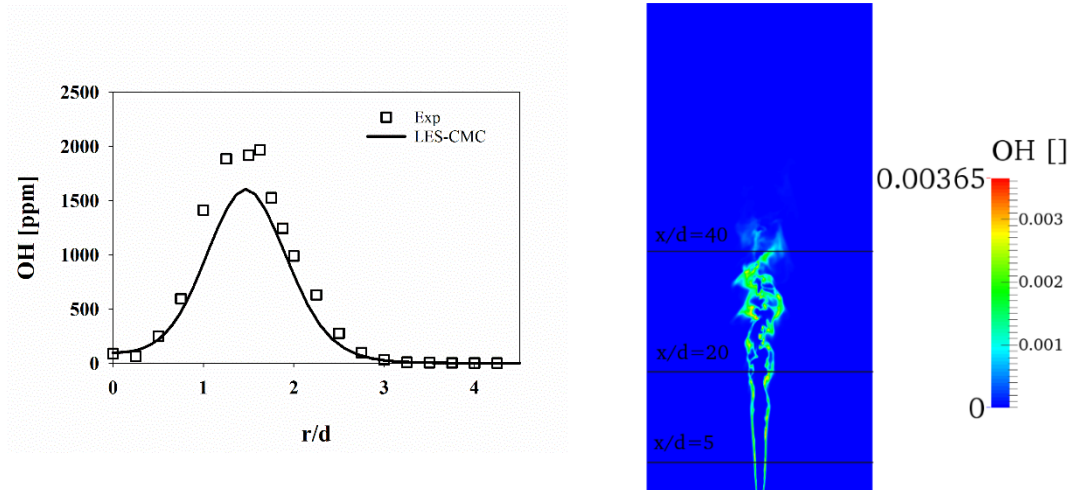
Figure 15. Right: Favre averaged *OH* mass fraction at location *x/d* = 20. Left: Instantaneous *OH* mass fraction contour plot.

Conclusions

CFD simulations, combining the LES/CMC approaches, have been presented for a turbulent non-premixed flame, with a mixture of hydrogen and nitrogen as fuel. The LES equations were solved using OpenFOAM, while an in-house finite-volume code (Garmory et al, 2013) was used for the CMC equations.

In order to illustrate the effect of turbulence, the Method of Random spot has been used as turbulent inlet boundary condition. With this method there is spatial correlation through the imposed length scale, but no temporal correlation in the imposed velocity fluctuations. Mean velocity profiles are in good agreement with experimental data. Along the centreline the error is always below the 10% . The rms velocity evolution along the centreline reveals that turbulence decays unrealistically near the nozzle. This reveals a limitation of the Random Spots method as implemented for the case at hand. Most probably the lack of temporal correlation between the random spots is the main cause. Compared to other methods for turbulence generation, such as the use of inlet profiles obtained from separate LES pipe flow simulations,

or the simulation of both burner and combustion chamber, the computational cost is much lower.

Through convection and diffusion, the turbulent flow field has a direct impact on the mixing field in terms of mean and rms. value of mixture fraction. On its turn this affects the results obtained for temperature and species mass fractions.

All results have been obtained without modelling of differential diffusion. Nevertheless, the analysis of the stoichiometric SDR along the centreline revealed that the mixing length scale is smaller than the Kolmogorov length scale until $x/d = 15$, which indicates the importance of differential diffusion in that region. Transport by turbulence dominates over molecular diffusion further downstream.

Acknowledgement

REFERENCES

Brown, P. N., Hinmarsh, A. C., 1989. Reduced storage matrix methods in stiff ode systems. *J. Comput. Appl. Math.,* **31**, 40.

Cristopher , J., 2015. *OpenFOAM User Guide.* [Online] Available at: http://www.openfoam.org/docs/OpenFOAM Documentation

D'Ausilio, A., Stankovic, I., Merci., B. 2017. Study of a turbulent nitrogen-diluted hydrogen-air diffusion flame through Large Eddy Simulations coupled with a first order conditional moment closure method. *Int. Symposium on Advances in Computational Heat Transfer,* 1783.

Davidson, L., 1997. LES of Recirculating Flow Without any homogenous direction: A Dynamic One-Equation Subgrid Model. *2nd Int. Symposium on Turbulence Heat and Mass Transfer*, 481.

Ertesvag, I. S., Magnussen, B. F., 2000. The Eddy Dissipation turbulence energy cascade model. *Combust. Sci. Technol.,* **159**, 213.

Forkel, H., Janicka, J., 2000. Large Eddy simulation of a turbulent hydrogen diffusion flame. *Flow, Turbulence and Combustion,* **65**, 163.

Garmory, A. & Mastorakos, E., 2013. Sensitivity analysis of LES-CMC predictions of piloted jet flames. *International Journal of Heat and Fluid Flow,* **39**, 53.

Garmory, A. & Mastorakos, E., 2011. Capturing localised extinction in Sandia Flame F with LES-CMC. *Proc. Comb. Inst.,* **33**, 1673.

Garmory, A. & Mastorakos, E., 2015. Numerical simulation of oxy-fuel jet flames using unstructured LES-CMC. *Proc. Comb. Inst.,* **35**, 1207.

Johnson, A. W., Sreenivasan, K. R., 1993. The thickness distribution of OH Regions in a Turbulent Diffusion Flame. *Combust. Sci. Tech.,* **89**, 1.

Klein, M., Sadiki, A., Janicka, J., 2003. A digital filter based generation of inflow data for spatially developing direct numerical or large eddy simulations. *Journal of Computational Physics*, **186 (2)**, 652.

Klimenko, A. Y., Bilger, R. W., 1999. Conditional moment closure for turbulent combustion. *Progress in Energy and Combustion Science,* **25**, 595.

Kornev, N. & Hassel, E., 2007. Method of random spots for generation of synthetic inhomogeneous turbulent fields with prescribed autocorrelation functions. *Communications in Numerical Methods in Engineering,* **23**, 35.

Li, J., Zhao, Z., Kazakov, A., Dryer, F., 2004. An Updated Comprehemsive Kinetic Model of Hydrogen Combustion. *International Journal of Chemical Kinetics,* **36**, 566.

Lund, T., Wu, X. & Squires, D., 1998. Generation of turbulent inflow data for spatially-developing boundary layer simulations. *Journal of Computational Physics,* **140**, 233.

Maragkos, G., Rauwoens, P., Merci, B., 2015. Assessment of a methodology to include differential diffusion in numerical simulations of a turbulent flame. *International Journal of Hydrogen Energy,* **40**, 1212.

Meier, W., Prucker, S., Chao, M. H., Stricker, W., 1996. Characterization of a turbulent H2/N2/air jet diffusion flames by single-pulse spontaneous raman scattering. *Combust. Sci. Technol.,* **118**, 293.

Meier, W., Vydorov, A. O., Bergmann, V. & Stricker, V., 1996. Simultaneous Raman/LIF measurement of makor species and NO in turbulent H2/air diffusion flames. J. *Appl. Phys.,* **63**, 79.

O'Brien, E. E., Jiang, T. L., 1991. The conditional dissipation rate of an initial binary scalar in homogeneous turbulence. *Phys. Fluids,* **3**, 3121.

Panjwani, B., Ertesvag, A., Gruber, A., Rian, K. E., 2010. Turbulence combustion closure model based on the Eddy dissipation concept for large eddy simulation. *Advances in Fluid Mechanics VIII,* **69**, 27.

Pera, C., Reveillon, J., Vervisch, L., Domingo, P., 2006. Modeling subgrid scale mixture fraction variance in LES of evaporating spray. *Combust. Flame,* **146**, 635.

Peters, N., 2000. *Turbulent Combustion.* Cambridge, UK: Cambridge University Press. Chap. 3. pp. 213-214

Pfuderer, D. G. et al., 1996. Turbulence Modulation in Jet Diffusion Flames: Modeling and Experiments. *Combust. Flame,* **106**, 302.

Pitsch, H., 2000. Unsteady Flamelet Modeling of Differential Diffusion in Turbulent Jet Diffusion Flames. *Combust. Flame,* **123**, 358.

Pitsch, H., Chen, M., Peters, N., 1998. Unsteady Flamelet Modeling of Turbulent Hydrogen-Air Diffusion Flames. *Twenty-Seventh Symposium (International) on Combustion, 1,* 1057.

Poinsot, T. & Veynante, T., 2005. *Theoretical and Numerical Combustion. 2* ed. Institut de Mecanique des Fluides Toulose: Edwards. Chap. 4. pp. 141-142

Pope, S. B., 2000. *Turbulent Flows.* 1 ed. Cambridge: University of Cambridge. Chap. 5. pp. 105-106.

Schmitt, T., Mery, Y., Boileau, M., Candel, S., 2011. Large-eddy simulation of oxygen/methane flames under transcritical conditions. *Proc. Comb. Inst.,* **33**, 1383.

Schumann, U., 1975. Subgrid scale model for finite differences simulation of turbulent flows in plane channels and anuli. *Journal Computational Physics,* **18**, 376.

Stankovic, I., Mastorakos, E., Merci, B., 2013. LES-CMC simulations of different auto-ignition regimes of hydrogen in a hot turbulent air co-flow. *Flow, Turbulence and Combustion,* **90**, 583.

Zhang, H. & Mastorakos, E., 2016. Prediction of Global Extinction Conditions and Dynamics in Swirling Non-premixed Flames Using LES-CMC. *Flow, Turbulence and Combustion,* **96**, pp. 863.